Investigating Mg-doping on ZnSnN2 ternary thin films via reactive magnetron co-sputtering

Aeshah Almushawwah, Hamad Albrithen, Joselito Labis, Mahmoud Al-Gawati, A.M. El-Naggar, Fahad Alnjiman, Jaafar Ghanbaja, Jean-François Pierson, Abdullah N Alodhayb

Materials Today Communications 51 (2026) 114671

Contents lists available at ScienceDirect

Materials Today Communications

journal homepage: www.elsevier.com/locate/mtcomm

Investigating Mg-doping on $ZnSnN_2$ ternary thin films via reactive magnetron co-sputtering

Aeshah Almushawwah [a,b], Hamad Albrithen [a,c], Joselito Labis [c], Mahmoud Al-Gawati [c], A.M. El-naggar [a], Fahad Alnjiman [a,d], Jaafar Ghanbaja [d], Jean-François Pierson [d], Abdullah N. Alodhayb [a,c,*]

[a] Department of Physics and Astronomy, College of Science, King Saud University, Riyadh 11451, Saudi Arabia
[b] Department of Physics, Faculty of Science and Humanities in Al-Dawadmi, Shaqra University, Shaqra 11911, Saudi Arabia
[c] Biological and Environmental Sensing Research Unit, King Abdullah Institute for Nanotechnology, King Saud University, P.O. Box 2455, Riyadh 11451, Saudi Arabia
[d] Université de Lorraine, CNRS, IJL, F-54000 Nancy, France

ARTICLE INFO

Keywords:
$ZnSnN_2$
III-V compound
$Zn–IV–N_2$
Ternary alloys
Magnetron co-sputtering

ABSTRACT

This study investigated Mg doping on $ZnSnN_2$ thin films via the magnetron co-sputtering technique under a high-purity nitrogen background at room temperature. Room-temperature deposition allowed assessment of intrinsic microstructural evolution without thermally driven diffusion, highlighting Mg-induced formation of Mg_3N_2 and Si–N-rich interfacial layers. The discharge power of the magnetron sputtering containing Mg target had the values 0, 120, 140, 160, 180, 200, 220, and 240 W, making eight thin films. In contrast, other growth conditions, such as the N_2 flow rate, discharge currents on the Zn and Sn targets, substrate temperature, and deposition time, were kept constant for all eight films; only the Mg power was varied. The microstructure and morphology, metallic bulk chemical composition ratios, and optical behavior of the deposited $ZnSnN_2$ thin films were examined by TEM, SEM, XRD, XPS, and Reflectance analysis, where the film properties indicate the formation of Mg_3N_2. Although Mg atoms did not seem to substitute in the lattice sites of $ZnSnN_2$, there is an indication of possible lattice-interstitial insertions, because of the noticeable changes in their sizes. As confirmed by XRD and cross-section TEM studies, adding Mg has affected grain sizes and resulted in the formation of a Si-N-rich layer at the film-substrate interface. These results provide insight into the role of Mg in defect and interface engineering of $ZnSnN_2$, offering new directions for display and optoelectronic applications.

1. Introduction

Ternary III–N alloys, such as the well-studied InGaN, are used in LED applications due to their promising optoelectronic properties. On the other hand, (Zn, Mg)–IV–N_2 alloys are also interesting materials due to their bandgap energies falling within the visible spectrum range, making them potential candidates for display technologies and LEDs. These advantages, therefore, make Zn–IV–N_2 and/or Mg–IV–N_2 promising alloys when combined with InGaN [1,2].

Among the Zn–IV–N_2 alloys of III–N materials, $ZnSnN_2$ is the most widely studied compound with various applications in optoelectronics [3,4]. $ZnSnN_2$ has a low optical bandgap (1–2 eV) compared to other Zn–IV–N_2 families such as $ZnGeN_2$ and $ZnSiN_2$ [5–8]. $ZnSnN_2$ is a II–IV–N_2 semiconductor that shares structural and electronic similarities with the III–V nitrides such as GaN and InGaN, owing to its wurtzite-derived orthorhombic lattice and direct, tunable bandgap. It has recently attracted attention as an earth-abundant, non-toxic alternative for optoelectronic and photovoltaic applications. Various dopants, including Al, Ga, and In, have been explored to tailor carrier concentration and bandgap; however, reports on Mg incorporation remain quite limited. Mg, as a group-II element, is of particular interest for introducing such an element and modifying electronic structure and energy levels. In this study, we investigate the effect of Mg co-sputtering power on $ZnSnN_2$ thin films grown at room temperature, providing new insights into Mg incorporation behavior, grain-structure evolution, and interfacial nitride formation.

The first theoretical study on $ZnSnN_2$ thin films was reported in 2008 by Paudel et al. [3], while Feldberg et al. reported the synthesis of $ZnSnN_2$ in 2012 [9]. Although $ZnSnN_2$ crystallizes into either orthorhombic or wurtzite structure, other structures, such as hexagonal or

* Corresponding author at: Department of Physics and Astronomy, College of Science, King Saud University, Riyadh 11451, Saudi Arabia,
E-mail address: aalodhayb@ksu.edu.sa (A.N. Alodhayb).

https://doi.org/10.1016/j.mtcomm.2026.114671
Received 22 September 2025; Received in revised form 7 January 2026; Accepted 12 January 2026
Available online 13 January 2026

monoclinic, were also reported [10–13].

Although the structure and lattice parameters of sputtered $ZnSnN_2$ film are difficult to determine via X-ray diffraction (XRD) due to the preferred orientation of the film, $ZnSnN_2$ ternary thin films can be deposited in pure nitrogen via magnetron sputtering. For instance, Deng et al. reported the deposition of ZnSnN2 thin films by DC magnetron sputtering [14], while Alnjiman et al. reported the growth of ZnSnN2 thin films under a working pressure of 1 Pa [1]. Moreover, $ZnSnN_2$ can be grown using separate metallic targets of zinc, tin, and magnesium, while others grow $ZnSnN_2$ thin films using a single target containing zinc–tin alloy. However, the separate-target approach has enabled better control of the film stoichiometry in the ternary structure [1,14,15].

On the other hand, another material in the II-IV-N_2 family, $MgSnN_2$, has been studied since 2016, as both Zn and Mg have two electrons in the outer shell belonging to the IIB and IIA groups, respectively, in the periodic table. The structure, lattice constants, and bandgap of $MgSnN_2$ were theoretically studied using DFT, QSGW, and the full-potential muffin-tin orbital method [16,17]. Kawamura *et al.* reported the successful synthesis of $MgSnN_2$ thin films via a metathesis reaction under high pressure, in which the resulting MgSnN2 had a rocksalt structure with a bandgap of $E_g = 2.3$ eV [18]. Alnjiman et al. grew wurtzite-like $MgSnN_2$ thin films via reactive magnetron co-sputtering with a tunable optical bandgap ranging from 2.28 to 2.43 eV [19]. Generally, disordered $MgSnN_2$ wurtzite structures exhibit a bandgap of 2.3–2.7 eV [20,21]. Yamada et al. explored the growth of $Mg_{1+x}Sn_{1-x}N_2$ alloys by depositing thin films on (001) GaN/c-Al_2O_3 substrates using reactive magnetron co-sputtering with Mg and Sn targets in a 1:4 Ar/N_2 gas mixture at 400 °C under a pressure of 1.0 Pa. The films formed wurtzite crystals and exhibited an intrinsic bandgap of approximately 2.3 eV [21]. Later, in 2021, the same group reported the deposition of $Mg_xZn_{1-x}SnN_2$ alloys on similar substrates, this time using $Mg_{0.4}Sn_{0.6}$ and $Zn_{0.6}Sn_{0.4}$ targets in a pure nitrogen environment [2]. These alloys, combining $MgSnN_2$ and $ZnSnN_2$ in a wurtzite-type structure, were identified as promising earth-abundant semiconductors with tunable band gaps ranging from 1.5 to 2.3 eV, depending on composition. By adjusting the deposition temperature to 300 °C and 400 °C, Zn-rich and Sn-rich films were selectively produced. The tunable bandgap behavior of $Mg_xZn_{1-x}SnN_2$, varying with composition (x from 0 to 1), further highlights its potential for optoelectronic applications [2].

As previously stated, $ZnSnN_2$ has a bandgap range from 1 to 2 eV [5–7], while $MgSnN_2$ with a disordered wurtzite structure has a bandgap of 2.3–2.7 eV [20,21]. Therefore, $Mg_xZn_{1-x}SnN_2$ thin films are expected to exhibit tunable wide bandgap ranging from 1 to 2.7 eV. Moreover, since the two systems have similar lattice structures, $Mg_xZn_{1-x}SnN_2$ ternary films are expected to be miscible, or homogeneous, across the entire *x* range for given growth temperatures.

As semiconductors with a direct bandgap between 1.8 and 2.5 eV are excellent candidates for LEDs and top cells in high-efficiency tandem solar cells, $Mg_xZn_{1-x}SnN_2$ is, therefore, expected to be a good candidate as an alternative material to $In_xGa_{1-x}N$, especially for high-indium alloys [2]. Despite the promising prospects of $Mg_xZn_{1-x}SnN_2$, the number of studies to date remains limited, underscoring the need for further investigations to clarify their optoelectronic properties.

Therefore, in this study, we investigated the growth of $ZnSnN_2$, $MgSnN_2$, and Mg-$ZnSnN_2$ thin films on Si substrates via magnetron sputtering at room temperature, with magnetron powers up to 200 W, to contribute to the understanding of the properties of MgZnSnN2 for display and LED applications.

2. Materials and methods

The $MgZnSnN_2$ thin films were deposited on intrinsic Si(001) substrates via reactive magnetron co-sputtering using high-purity 99.9 % Zn, Mg, and Sn metal targets in a pure 5 N nitrogen atmosphere. The diameter of the target was 50.8 mm, and the distance between the targets and the substrate holder was fixed at 90 mm. The substrate holder was a rotating Inconel-Molybdenum block with N_2 gas (99.999 % purity) flowing to provide reactive nitrogen species for the synthesis of $MgZnSnN_2$ films under N_2 plasma.

By controlling the power of a reactive magnetron radio frequency (RF) sputtering gun containing an Mg target, different amounts of magnesium ions were introduced into the N_2 plasma while simultaneously growing the $ZnSnN_2$ thin films. The effect of the sputtering gun's power on the physical and chemical properties of the deposited thin films is then investigated.

The powers used to sputter the Mg target (P_{RF}^{Mg}) were 0, 120, 140, 160, 180, 200, 220, and 240 W; corresponding to the samples named MMFC= 0 at%, MMFC= 8.7 at%, MMFC= 12.5 at%, MMFC= 17.2 at%, MMFC= 19.7 at%, MMFC= 24.7 at%, MMFC= 27.1 at%, and MMFC= 28.9 at%, respectively. Other sputtering deposition parameters were fixed. N_2 flow rate was fixed at 30 sccm, Zn current (C_{DC}^{Zn}) at 0.1 A, and Sn current (C_{DC}^{Zn}) at 0.25 A. Furthermore, the working pressure was fixed at 1 Pa, and the deposition time for each sample was 10 min. The deposition of the reference $ZnSnN_2$ film was performed as described in the literature [1], where the working pressure of 1 Pa in nitrogen (N_2) atmosphere was expected to be crucial in producing highly crystalline thin films with stoichiometry close to the ideal stoichiometric ratio (1:1:2) [1].

The structural, elemental, and optical properties of the resulting MgZnSnN2 films were characterized by θ-2θ XRD measurements using the Bruker D8 Advance Diffractometer with a Cu anode (λ_{Cu} $K_{\alpha 1}$ = 1.5406 Å). At the same time, the morphology was imaged via JEOL JSM-7600F Field-Emission Scanning Electron Microscopy (SEM), equipped with Energy Dispersive X-ray Spectroscopy (EDX), and operated at 5 kV in SEI (secondary electron imaging) mode, and Transmission Electron Microscopy (TEM) using the JEOL ARM 200 F Cold-FEG TEM/STEM operating at 200 kV. The TEM is equipped with a spherical aberration (Cs) probe corrector, providing a point resolution of 0.12 nm in the TEM mode and 0.078 nm in the STEM mode. The reflectance measurements were executed using a computer-aided double-beam spectrophotometer (Cary 5000 from Varian) with a VW-shaped absolute specular reflectance accessory (SRA). All samples were measured at an incidence angle of 5.0 ± 0.1° to avoid fringe shifts caused by angular discrepancies. The chemical bonding states and surface compositions of the MZSN thin films were investigated via X-ray Photoelectron Spectroscopy (XPS, JEOL 9030) with Al/Mg Kα X-ray sources operated at 300 W (12 kV and 25 mA), 100-ms dwell time, and 0.1 eV step energy, and 10 eV pass energy, was employed to determine the surface chemical nature of the films. All data were calibrated and corrected by Au 4 $f_{7/2}$ at 83.3 eV and C 1 s at 284.2 eV with a correction of ~0.5 eV. The high-resolution XPS spectra of N 1 s, Zn 2p, Sn 3d, and Mg 2 s were analyzed. Although all thin films were characterized, the results of only three are shown for conciseness.

3. Results and discussion

The magnesium (Mg) content for each sample was measured by energy-dispersive X-ray spectroscopy (EDX) and reported as the Mg Metallic Fraction Concentration (MMFC). Fig. 1 shows how the composition of $MgZnSnN_2$ films changes with different levels of Mg sputtering power. The EDX spectra of Fig. (a-h) clearly reveal that the intensity of the Mg peak increases with higher Mg target power, while the peaks for zinc (Zn) and tin (Sn) remain essentially unchanged. This indicates that Mg is being successfully incorporated into the films without significantly impacting the Zn and Sn signals.

Fig. 1(i) presents the corresponding quantitative elemental analysis. The Mg concentration increases consistently as sputtering power increases. At the same time, the concentrations of Zn and Sn show a slight decline, suggesting that Mg may be substituting for Zn and/or Sn within the cation sublattice. The insert in Fig. 1(j) on the right side further supports this interpretation. It shows that the Zn:Sn atomic ratio remains

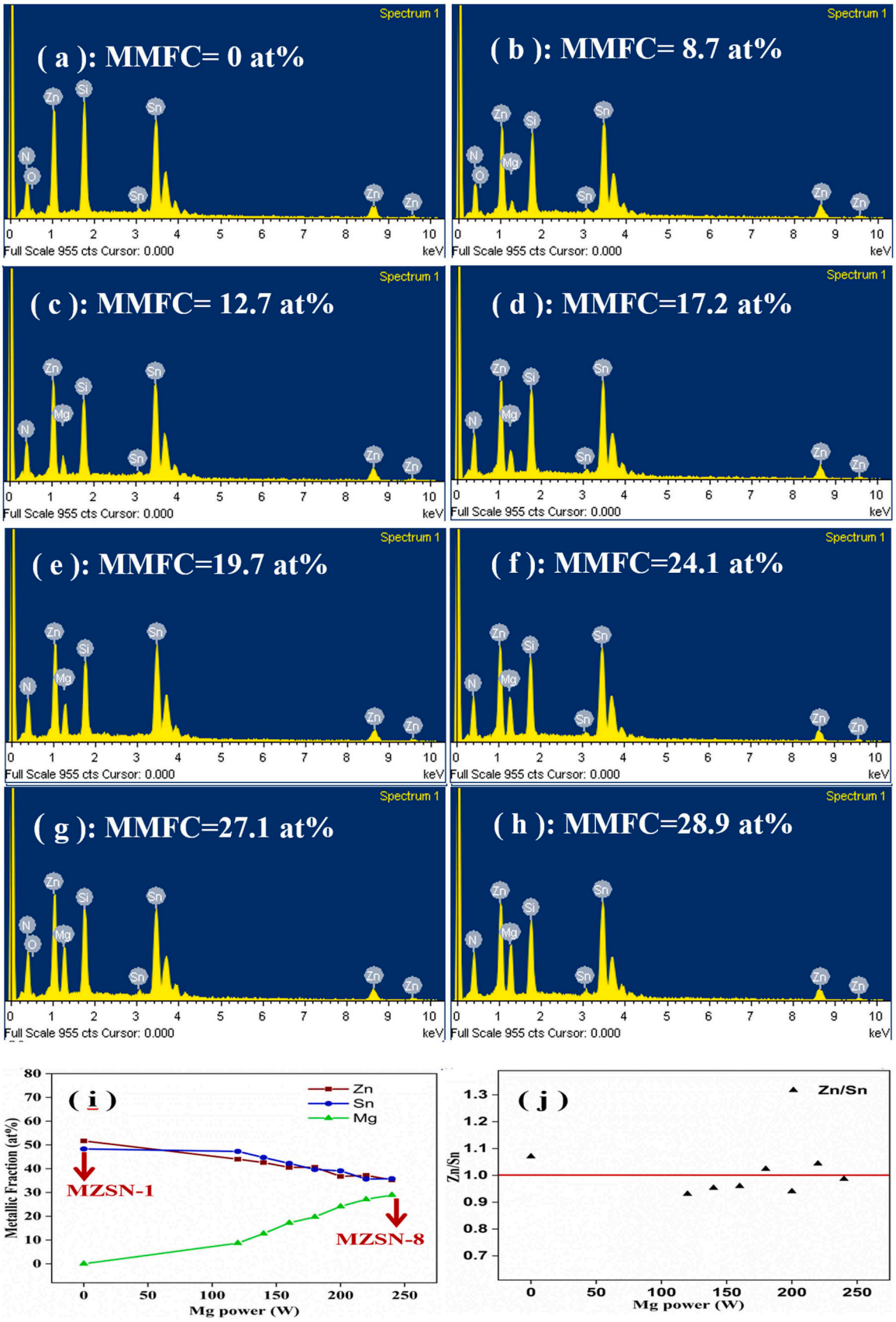

Fig. 1. (a-h): EDX spectra of $MgZnSnN_2$ films grown under Mg-target RF powers of (a) 0, (b) 120, (c) 140, (d) 160, (e) 180, (f) 200, (g) 220, and (h) 240 W, showing progressive enhancement of Mg peaks with increasing power; (i) Quantitative Mg, Zn, and Sn concentrations plotted as a function of Mg sputtering power; (j) associated with the right-side plot: Zn/Sn atomic ratio versus Mg-target power, demonstrating stable Zn-Sn stoichiometry despite varying Mg incorporation.

nearly constant across all Mg power levels, maintaining a consistent 1:1 ratio. This stability implies that the base $ZnSnN_2$ stoichiometry is preserved during Mg incorporation, likely through substitution rather than disruption of the Zn-Sn framework. Further structural studies are required to elucidate the precise mechanism of Mg incorporation.

Fig. 2 shows the XRD patterns of the deposited $ZnSnN_2$ thin films. The grown films exhibit a polycrystalline nature with grains oriented in different directions. The XRD patterns show five distinguishable peaks. The Si 002 peak, denoted by (*), corresponds to the Si substrate. The peaks at around 34° (Mg_3N_2 321, denoted by a dot) appear only in films with Mg content and are attributed to Mg_3N_2 grains with small crystallites [22]. These peaks are more apparent in films with MMFC more than 10 %. The other peaks denoted by (002), (122), and (123) are attributed to $ZnSnN_2$. A slight increase in XRD at a slightly higher angle near the Mg_3N_2 (321) peak is attributed to the presence of pure Mg (002) reflection. Although the peak is too weak, it suggests the possible coexistence of unreacted Mg minute clusters within the film.

Single-phase $Mg_xZn_{1-x}SnN_2$ thin films are theoretically expected to have XRD peaks with 2θ positions between those of $ZnSnN_2$ and $MgSnN_2$. However, the main characteristic peaks observed in our experimental data closely match those previously reported for $ZnSnN_2$ [14,23,24]. This indicates that the $ZnSnN_2$ phases observed in this study correspond to either the orthorhombic [8,14,23] or the wurtzite [24] structure. Notably, our XRD results do not show any significant shifts with increasing Mg concentration, as would be expected if Mg were being incorporated into the $ZnSnN_2$ lattice to form $MgZnSnN_2$. This suggests that Mg ions are not substantially incorporated into the $ZnSnN_2$ lattice in our films. As the Mg concentration increases, a peak associated with magnesium nitride (Mg_3N_2) becomes more pronounced, indicating the formation and coexistence of Mg_3N_2 grains alongside $ZnSnN_2$. However, the presence of Mg_3N_2 does not appear to disrupt the $ZnSnN_2$ lattice structure, as further evidenced by the stability of the (002) peak position. While this peak could potentially be attributed to ZnO (111), due to its alignment with known ZnO diffraction data and the possibility of Zn reacting with oxygen, this interpretation is not supported by optical reflectance analysis (see Fig. 8). The analysis shows no decrease in the refractive index with increasing Mg content, which would be expected if ZnO were present. This finding further supports the conclusion that the observed peak originates from the $ZnSnN_2$ structure rather than ZnO formation.

Fig. 3a shows the main (002) peak positions as a function of MMFC, and Fig. 3b their corresponding interplanar spacings. Adding Mg can cause a strain in the structure, which could explain the minute shifts in the positions of the observed peaks compared to the previously reported data [18]. However, the main 002 peak positions did not noticeably change as Mg contents increased, while the interplanar spacings did not match the increasing Mg in the films. Although this behavior indicates possible stress-induced lattice changes, the absence of apparent peak shifts does not exclude minor Mg substitution below the detection limit of conventional XRD. It is therefore possible that Mg atoms occupy interstitial or grain-boundary positions, although further confirmation through high-resolution STEM-EDS or Rietveld refinement would be required. The observed grain-size reduction and weaker (002) orientation may arise from Mg-induced modifications in surface diffusion and adatom mobility, consistent with dopant-induced surface-energy effects reported in GaN systems. Ramachandran et al. reported that GaN growth by molecular beam epitaxy (MBE) on 6H-SiC(0001) substrates resulted in Ga-polar GaN (0001) [25]. However, when the surface was exposed to Mg flux, the polarity reversed, leading to the formation of nitrogen-polar GaN(0001). This finding suggests that Mg can influence the growth polarity in nitride systems. It is important to note that in the case of GaN, both Ga- and N-polar orientations are constrained by the three-fold symmetry of the substrate, which enforces a specific growth direction. In contrast, the films in our study were not grown epitaxially, implying that the absence of substrate-imposed symmetry likely reduced the energy barriers associated with various growth orientations. Moreover, Bungaro et al. conducted *ab initio* calculations to investigate Mg incorporation in GaN [26]. Their findings revealed that Mg incorporation is strongly dependent on the surface orientation and specific lattice sites of GaN. Additionally, the mode of Mg incorporation or potential segregation is influenced by the chemical potential nature of all constituent elements during growth [26]. These insights support our hypothesis that the observed reduction in the intensity of the (002) XRD peak may be a consequence of Mg promoting the growth of alternative crystallographic orientations at the expense of the (002) orientation, a trend further supported by the SEM analysis discussed later (as shown in SEM images in Fig. 6). Indeed, additional $ZnSnN_2$ peaks, particularly the (122) and (123) reflections, began to appear in the XRD patterns of Mg-containing films. These peaks were absent in the Mg-free reference film, suggesting that Mg incorporation may initiate or stabilize the formation of these orientations. Such structural changes could result from Mg's influence during the initial nucleation at the film-substrate interface or during subsequent film growth.

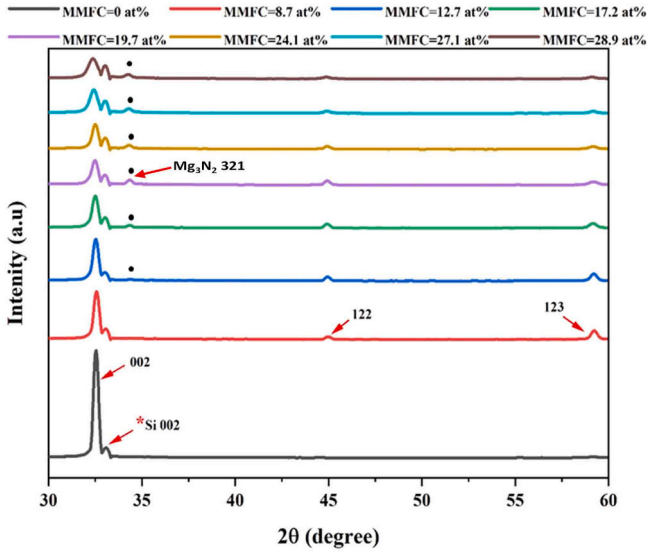

Fig. 2. XRD patterns of the sputtered $ZnSnN_2$ thin films at different Mg concentrations.

Fig. 4 shows the plot of grain size (D) as a function of MMFC. The average grain size is estimated using the Scherrer formula below:

$$D = \frac{(0.9)\lambda}{\beta \cos\theta} \quad (1)$$

where λ is the X-ray wavelength, β is the full width at half maximum (FWHM) in radians, and θ is the diffraction angle in radians. The analysis was performed for the first peak of 002 ($2\theta = 32.5°$). As observed, the grain sizes decrease approximately linearly with increasing Mg content, from 25.4 nm (MMFC = 0) to 15.5 nm (MMFC = 28.9 %). The reduction of $ZnSnN_2$ grain due to the increasing Mg concentration could be attributed to the coexistence of two types of crystallites, as well as to the possibility that some of the Mg atoms residing in the grain boundaries of $ZnSnN_2$ might limit the grain growth. These findings further support that the growth of 002 orientation is becoming energetically less favorable with the addition of Mg atoms, since growth at the surface of the substrate starts when all metals (Sn, Zn, and Mg) from sputtering start to nucleate. As there is a slight shift towards lower angles due to increasing Mg concentration in the films, this is accordingly reflected in a slight increase in the lattice constants (Fig. 3b). However, this change in the lattice constant is so small that, even accounting for the Mg concentration, a significant rise is still measured by EDX.

Fig. 5 shows the thicknesses of the $ZnSnN_2$ films as a function of MMFC. The study also investigated the effect of film thickness on grain

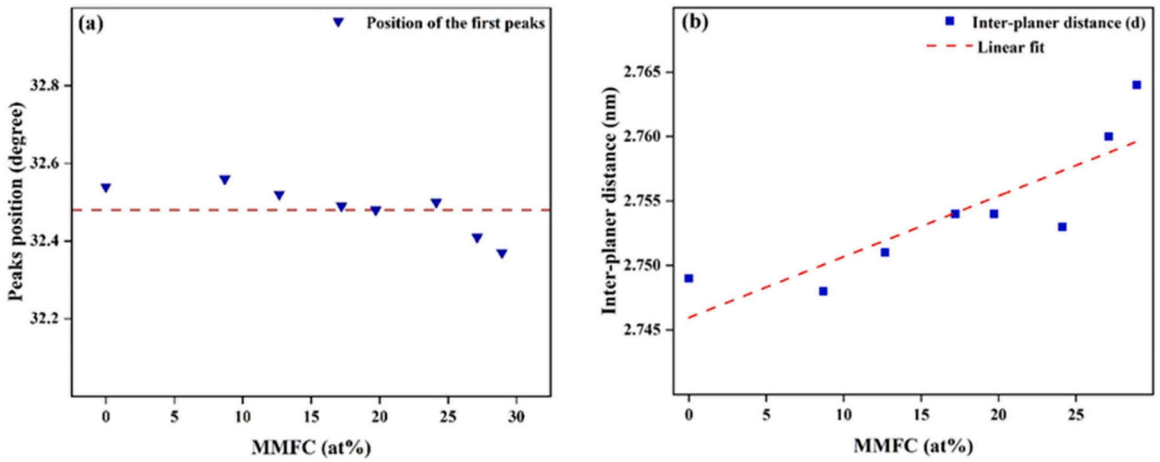

Fig. 3. (a) Positions of the first diffraction peak (002) and (b) the interplanar spacings as a function of MMFC.

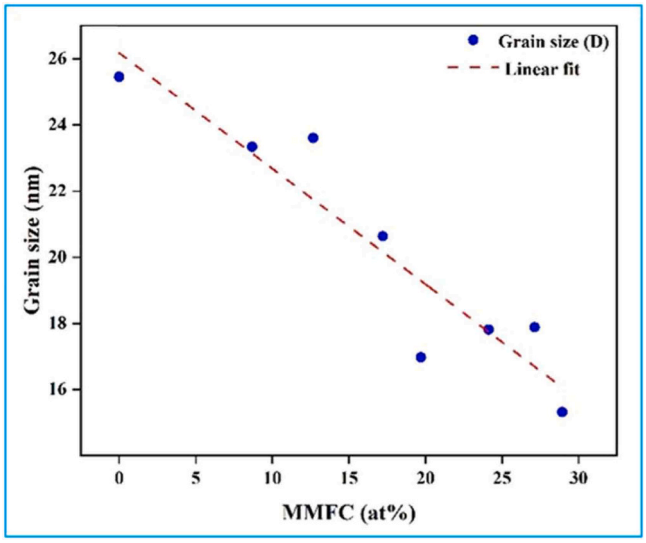

Fig. 4. $ZnSnN_2$ grain size as a function of MMFC.

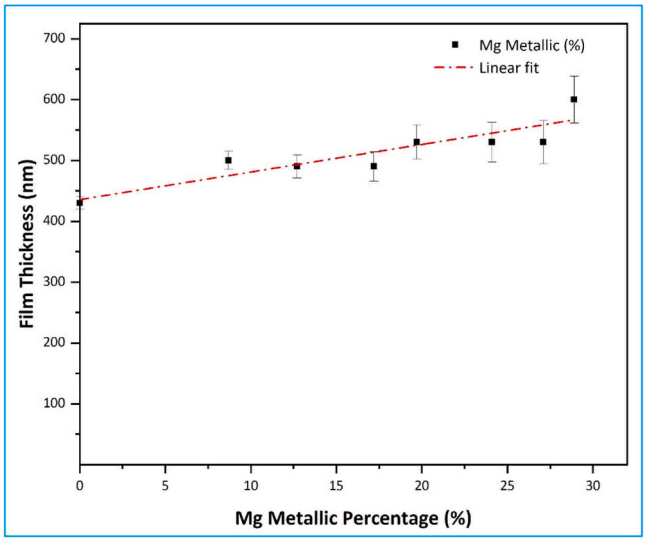

Fig. 5. Thickness of $ZnSnN_2$ films as a function of MMFC.

size, as measured by XRD for the (002) orientation. As shown in Fig. 5, the film thickness increases with increasing Mg concentration, suggesting that the decrease in grain size is not accompanied by a reduction in film thickness, thereby supporting our explanation of grain orientation preference. Logically, grain size is expected to increase with the addition of more materials and thus the thickness, but this is not observed here.

Fig. 6 shows the SEM images of the deposited thin films. All samples exhibit dense microstructures composed of uniformly distributed small grains. While the grain shapes remain generally consistent across the Mg-containing films, a slight variation in grain size is observed with increasing MMFC. In the reference film without Mg (MMFC = 0 at%, Fig. 6a), the grains appear smaller and more densely packed than in the Mg-doped samples (Fig. 6b–h), suggesting that Mg incorporation influences grain growth orientation. This observation qualitatively supports the hypothesis that (002)-oriented grains tend to grow more laterally with Mg addition, resulting in a reduction of their vertical dimension. The emergence of additional XRD peaks corresponding to the (122) and (123) planes with increasing Mg content further indicates a tilting of the (002) grains, possibly due to changes in growth orientation. This shift in growth mode may promote the formation of larger or coarser grains in films with higher Mg content. It is also worth noting that the (122) and (123) XRD peaks remain relatively weak, which may be attributed to the crystallographic mismatch between these orientations and the Si(001) substrate. The TEM imaging technique was also employed to image and study the interface area of the $ZnSnN_2$ thin films on Si substrates.

Fig. 7a-b show the TEM images for the MMFC= 8.7 % and MMFC= 28.9 % samples, respectively. The thickness of the MMFC= 8.7 % sample is lower than that of the MMFC= 28.9 %, which agrees with the thickness measurements shown in Fig. 5. The bright spots, indicated by black dashed circles in Fig. 7a-b are indicative of the grains in (002) orientation, since the high symmetry of the grains allows higher transmission of electrons. Further, the average grain size is larger in samples with low Mg concentration. Upon direct observation by TEM and correlation with XRD data obtained by the Debye-Scherrer method, a qualitative agreement in the Mg-incorporation size-dependent behavior is noticeable. TEM and XRD results provide support that Mg incorporation in the $SnZnN_2$ system reduces the size of (002)-oriented grains, thus limiting their vertical growth. Fig. 7c shows a magnified TEM image of the MMFC = 8.7 % sample, while Fig. 7d displays a depth-profile plot of the elemental analysis by the EDX-TEM system at various points in the interface (shown in blue-green dots). As seen in Fig. 7c, the grain has a well-ordered lattice spacing with a distance of 5.4 Å, which matches well with the (002)-interplanar spacing of 2.747 Å as extracted by XRD, as shown in Fig. 4b. Therefore, this lattice spacing of 5.4 Å can

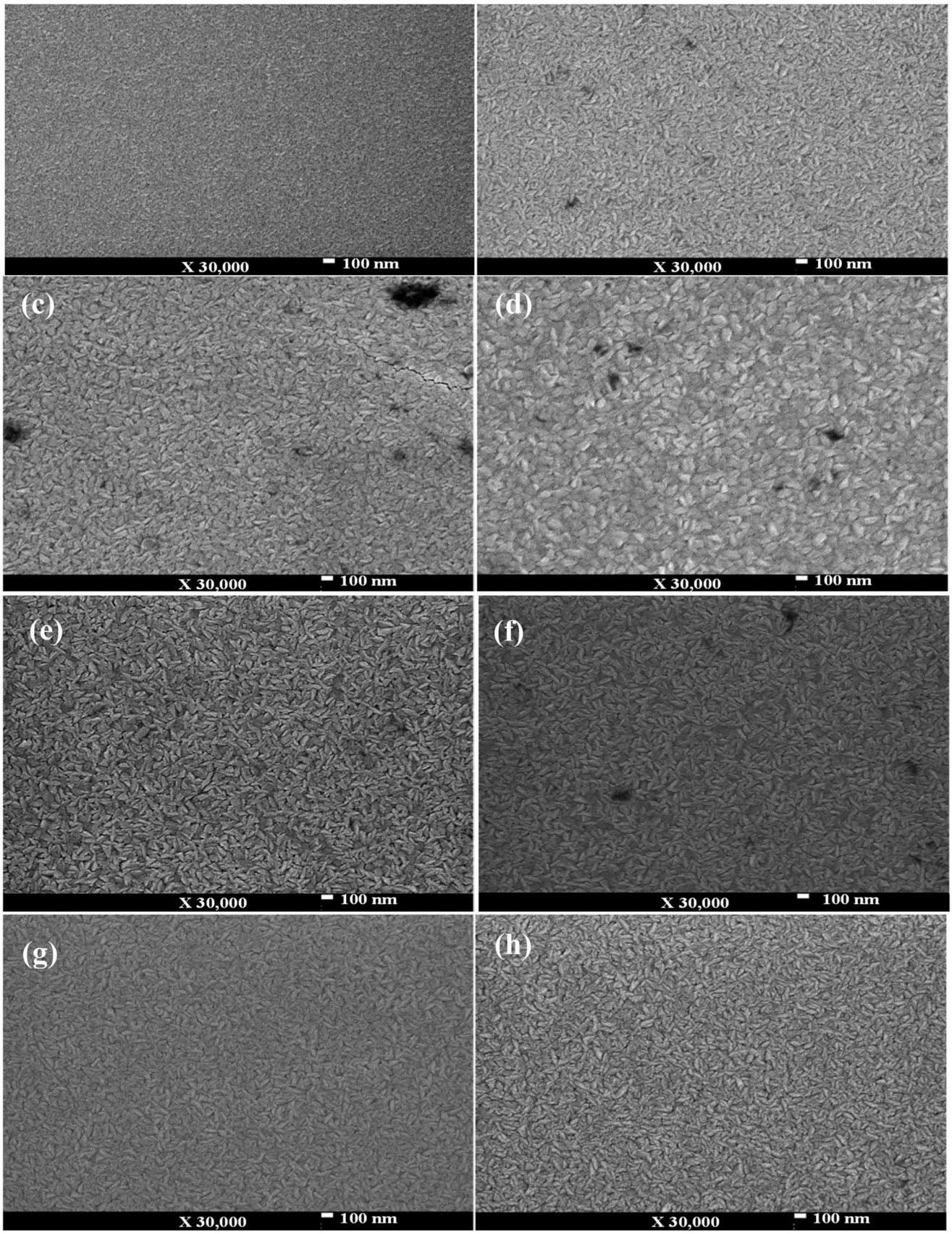

Fig. 6. SEM images of $ZnSnN_2$ thin films deposited under controlled conditions at different MMFC values: (a) 0, (b) 8.7, (c) 12.7, (d) 17.2, (e) 19.7, (f) 24.1, (g) 27.1, and (h) 28.9 at%.

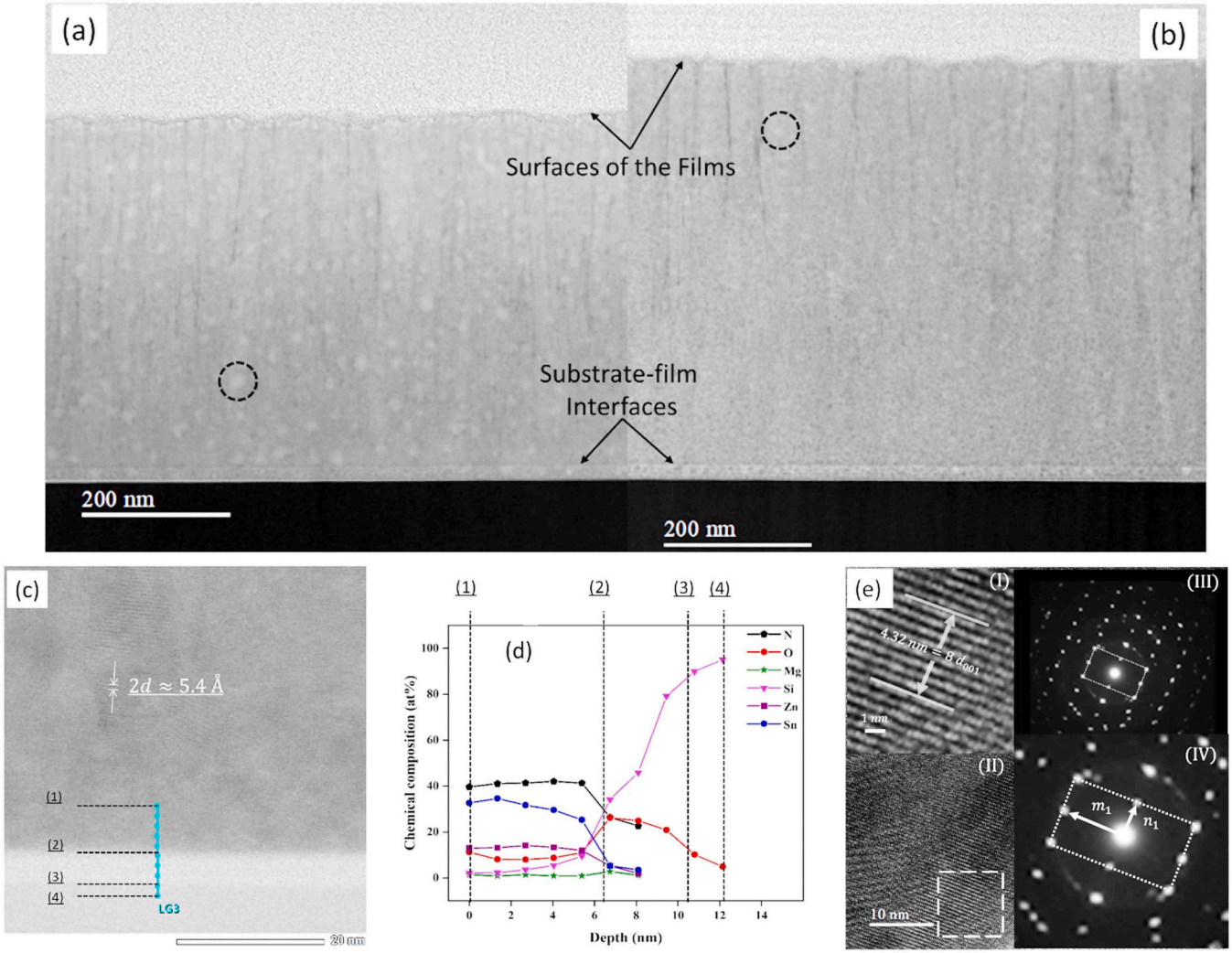

Fig. 7. HRTEM images of (a) MMFC = 8.7 % and (b) MMFC = 28.9 % samples. Fig. 7c is the magnified cross-section TEM image of the MMFC= 8.7 % sample. In comparison, Fig. 7d is the elemental analysis at the film-substrate interface region for MMFC= 8.7 % as a function of depth corresponding to the depth shown (blue-green dots) in Fig. 7c. Fig. 7e(I) shows a zoom-in image of the dashed square in Fig. 7e(II) of the MMFC= 8.7 %. In contrast, Fig. 7e(III) shows the SAED of 7e(II), and Fig. 7e(IV) shows a zoom-in SAED pattern of Fig. 7e(II).

be attributed to the related (001)-oriented $ZnSnN_2$ crystallites.

The interface region can primarily be sectioned by three layers: (a) thin film (above line 2), (b) intermediate layer (between 2 and 3), and (c) substrate (below line 3). EDX performed element point-mapping in each layer to analyze the chemical composition of each layer.

In the first layer (bottom layer) of the thin film, the concentration of Sn is higher than Zn, even though their Zn:Sn ratio is close to unity. This suggests that nucleation occurs on the lower part of the film, as its stoichiometry differs from that of the film. Furthermore, Mg concentration in this region is notably low, indicating limited Mg incorporation during the initial stages of film growth.

In the second layer (intermediate layer), an interesting trend emerges: the concentrations of Zn, Sn, and Mg are all significantly reduced (excluding nitrogen). This region is predominantly composed of nitrogen, oxygen, and silicon, with the Si concentration increasing progressively toward the third layer. These observations imply the formation of silicon nitride (Si–N) compounds that may extend into the first layer, influencing early film growth and interface chemistry.

In the third layer, corresponding to the substrate, nitrogen and Si–N compounds are anticipated in the upper portion. A reaction between N and Si to form N–Si compounds is possible under the current deposition conditions, as nitrogen can diffuse into the substrate and react with silicon [24,25].

In Fig. 7e, the atomic order is clearly visible, with a spacing of 4.32 nm across 8 consecutive layers. This means that the spacing is 5.4 $\AA$, in close agreement with the reported lattice parameter c of $ZnSnN_2$. Fig. 7e(III-IV) exhibits the reciprocal space of the lattice ordering with a rectangular symmetry indicated by the dotted rectangles in both images. The arrows denoted by n_1 and m_1 are the base vectors of the SAED patterns. It is observed that the ratio of the lattice constants $\left(\frac{c}{a}\right) = 0.94$, which is equal to the ratio of the reciprocal vectors $\left(\frac{m_1}{2n_1}\right)$. This is, in fact, consistent with the fact that the vector n_1 represents 002 order since 001 cannot be seen due to destructive interference. Indeed, the lattice parameters c and a are perpendicular to each other as well as their reciprocal vectors n_1 and m_1, respectively, as seen in Fig. 7(e-IV).

Reflectance measurements were also conducted to examine the optical properties of the Mg-$ZnSnN_2$ thin films. Fig. 8 shows the Reflectance spectra of the samples, each indicated by a different color. The angle of incidence was 0° for all measurements. All films exhibit interference patterns that oscillate between destructive and constructive interference. As the concentration of Mg increases, the amplitudes of the constructive interference increase. Moreover, the wavelengths of the interference fringes have shifted towards longer wavelengths.

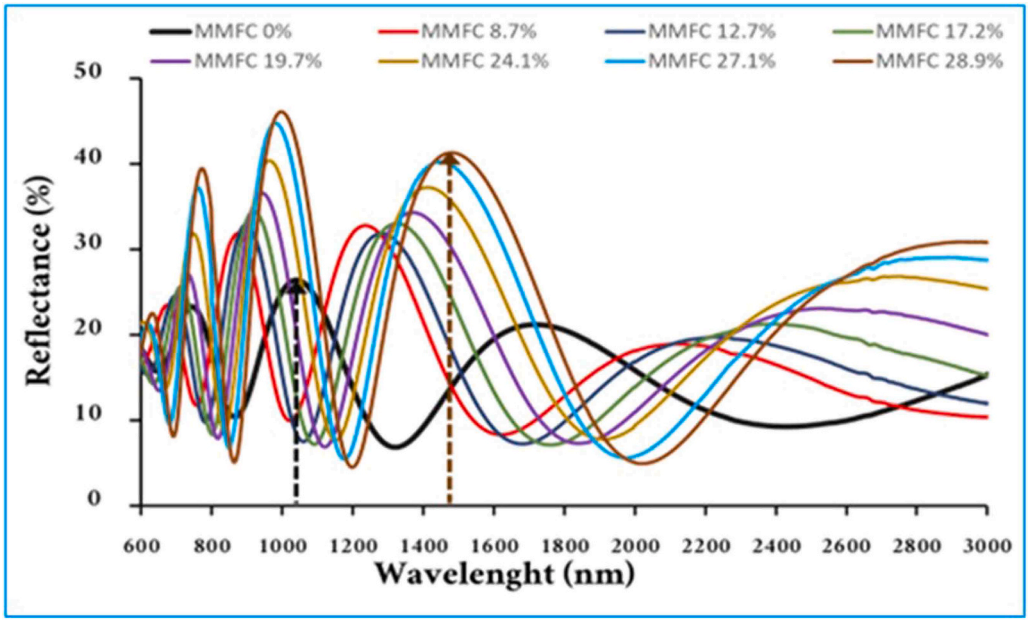

Fig. 8. Reflectance spectra of Mg-$ZnSnN_2$ thin films at MMFC at 0 (black), 8.7 (red), 12.7 (dark blue), 17.2 (green), 19.7 (violet), 24.1 (green-brown), 27.1 (light blue), and 28.9 (brown)%.

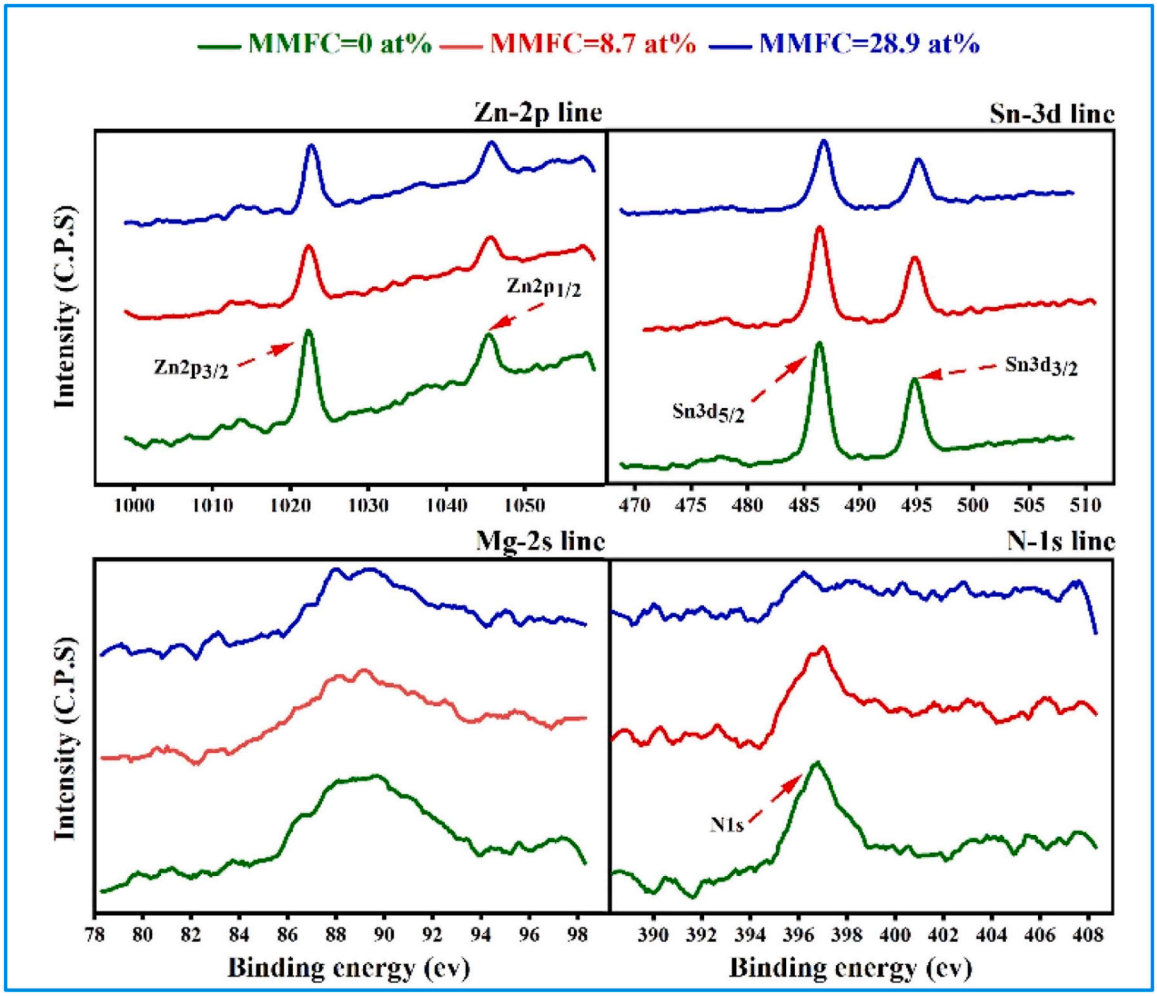

Fig. 9. High-resolution XPS spectra of Zn 2p (upper left), Sn 3d (upper right), Mg 2 s (lower left), and N 1 s (lower right) for Mg-$ZnSnN_2$ thin films with MMFC values: 0 (green), 8.7 (red), and 28.9 (blue) at%.

Comparing the MMFC= 0 % sample with the MMFC= 28.9 % sample, a clear difference can be observed. This can be explained below as follows.

$ZnSnN_2$ and Mg_3N_2 have close values of indices of refraction; Mg_3N_2 index of refraction is about 10 % higher than that of $ZnSnN_2$ [14,27]. Moreover, films with higher Mg content are thicker, as shown in Fig. 5. Therefore, both effects, higher thickness and index of refraction, contribute to the shift of interference peaks toward higher wavelength. In fact, the significant shift in the interference constructive peak between the sample with no Mg and the sample having the least Mg-content is affected mainly by the thickness difference. As observed, the amplitude of constructive interference increases with increasing Mg content, which is attributed to the presence of Si-N at the film-substrate interface. This material has a refractive index below that of $ZnSnN_2$ (as shown in Fig. 7), meaning that films with higher Mg content would reflect more light from the substrate-film interface as the refractive index difference increases. Moreover, by considering the film surface-air interface, a similar analogue can also contribute to an increase in reflected light. As expected, films with higher MMFC have higher reflectance. Hence, the optical reflectance results presented here are consistent with the data from EDX, XRD, Thickness profile, and HRTEM-EDX, as shown in Figs. 1, 2, 5, and 7, respectively.

Fig. 9a shows two peaks in the XPS spectrum of Zn $2p_{1/2}$ and 2 $P_{3/2}$. The stronger peak was ascribed to the Zn $2p_{3/2}$ and the weaker peak to the Zn $2p_{1/2}$ transition. With increasing MMFC, the position of the Zn $2p_{3/2}$ peak was observed to shift from 1022.3 to 1022.8 eV, while the Zn $2p_{1/2}$ peak shifted from 1045.4 to 1045.9 eV, which could be attributed either to energy corrections or the Zn–N bonds. However, Chinnakutti et al. reported positions of 1021.5, 1021.7, and 1021.4 eV for the Zn $2p_{3/2}$ peak and 1045.6 and 1045.5 eV for the Zn $2p_{1/2}$ peak, which are similar to those observed in the present study [23]. These peaks are associated with Zn–N bonding in $ZnSnN_2$ thin films, in good agreement with our results and those of other studies [23,28,29]. However, the first peak (1022.3 eV) was quite far from the reported value of 1021.3 eV, which could be attributed to the presence of Zn–O bonds (1022.4 eV) in the films, because Zn strongly interacts with O due to the high mutual affinity of Zn and O, thus explaining the first peak. Nonetheless, further investigation is needed to elucidate this result [30]. These XPS results indicated strong Zn peaks, suggesting the presence of Zn–N bonds on the film surface.

Fig. 9b also shows the high-resolution XPS spectra of Sn 3d. By considering the peak height ratios, two main Sn peaks were identified: the strong peak corresponding to Sn $3d_{5/2}$ and the weak one corresponding to Sn $3d_{3/2}$. Notably, the binding energy of the strong peak, which was ascribed to the Sn–N bonds in $ZnSnN_2$, shifted from 486.3 to 486.7 eV, which could be attributed to the incorporation of Mg with increasing content, thus affecting the Sn–N bonds [23,31]. Meanwhile, the weak peak also shifted from 494.8 to 495.1 eV with increasing Mg content. Owing to the weak interaction between Sn and O, the presence and shifting of Sn peaks could be attributed to the incorporation of Mg in the system, which affected the Sn–N bonds, as observed in the case of the strong peak. Although the peak shifts require further investigation, XPS data indicate the presence of Sn on the film surface.

Fig. 9c further shows the high-resolution XPS spectrum of Mg 2 s, which exhibits a broad peak between 93 and 86 eV. Instead of the Mg $2p_{3/2}$ line, the Mg 2 s line is presented because the Mg $2p_{3/2}$ peak shows a lower cross-section and occurs near the Fermi edge. Although MMFC= 0 at% shows a much broader central peak, which can be attributed to background and satellite peaks, the corresponding peaks for other MMFC appear narrower and shifted, possibly indicating Mg incorporation, as previously reported in other data. After curve-fitting (not shown), the peaks of Mg 2 s were positioned in the region of 88.6–89.2 eV, which is a typical characteristic of the Mg 2 s line. Although Mg may not be clearly observed on the film surface, the observed humps could have originated from sublayers beneath the surface.

Additionally, the XPS N 1 s spectra shown in the lower right of Fig. 9 exhibit a shift in the binding energy peak from 396.2 eV to 397.0 eV. This binding-energy range is consistent with values previously reported for tin nitride (SnN_x) thin films [32]. In $ZnSnN_2$ thin films, N 1 s binding energies in the range of ~396–397 eV have commonly been attributed to nitride nitrogen coordinated with Zn, corresponding to N–Zn bonding environments within the $ZnSnN_2$ lattice [1,23,32,33]. In particular, Choi *et al.* demonstrated that N 1 s peaks near 397 eV originate from strong Sn–N bonding formed under nitrogen-rich sputtering conditions [32], supporting the assignment of the observed peak shift to the combined presence of N–Zn and N–Sn bonds in the $ZnSnN_2$ thin films studied here. More importantly, the changes in the intensity of the N 1 s peak with increasing Mg content suggest a weak N presence at the film surface. Thus, the N 1 s signals can only be attributed to the presence of strong N-related bonds in the subsurface layers of the film. Although Yamada *et al.* reported XPS results for the O peaks, no prior studies have reported XPS data for the Zn, Sn, Mg, and N peaks of $Mg_xZn_{1-x}SnN_2$ at 34° (2θ), necessitating further investigation of this system [2].

4. Conclusions

In this study, Mg-$ZnSnN_2$ thin films were deposited via reactive magnetron co-sputtering at room temperature to investigate the effects of Mg incorporation on structural, interfacial, and optical properties. The powers of the reactive magnetron sputtering system with a Mg target varied from 0 to 220 W. In contrast, nitrogen (N_2) flow rates, discharge currents on the Zn and Sn targets, substrate temperatures, and deposition times were maintained constant. Despite a progressive increase in Mg flux with sputtering power, the $ZnSnN_2$ lattice parameters remained essentially unchanged, indicating minimal Mg substitution. Instead, Mg predominantly formed separate Mg_3N_2 crystallites coexisting with the $ZnSnN_2$ phase, as confirmed by stable XRD peak positions and high-resolution TEM imaging. Further, increasing Mg content to 28.9 % increased the film thickness without altering the $ZnSnN_2$ crystal structure, while reducing grain size and inducing secondary orientations due to altered growth kinetics. Higher Mg levels also led to thicker films and the formation of a Si-N interfacial layer due to nitrogen diffusion into the substrate. These changes, along with the higher refractive index of Mg_3N_2, enhanced reflectance and redshifted optical interference features. XPS showed stable Zn-N and Sn-N bonding, with minor chemical-state shifts at higher Mg flux. Overall, Mg incorporation at room temperature drives secondary-phase formation and interfacial reactions rather than lattice substitution, offering insights for tuning interfaces and defects in $ZnSnN_2$-based optoelectronics.

CRediT authorship contribution statement

Jaafar Ghanbaja: Writing – review & editing, Writing – original draft, Methodology, Investigation. **naggar A.M.:** Writing – review & editing, Writing – original draft, Supervision, Formal analysis. **Fahad Alnjiman:** Writing – review & editing, Writing – original draft, Methodology, Investigation. **Joselito Labis:** Writing – review & editing, Writing – original draft, Software, Methodology, Data curation. **Mahmoud Al-Gawati:** Writing – review & editing, Writing – original draft, Supervision, Methodology, Formal analysis, Data curation. **Aeshah Almushawwah:** Writing – original draft, Validation, Methodology, Formal analysis. **Hamad Albrithen:** Writing – review & editing, Writing – original draft, Methodology, Investigation, Formal analysis, Data curation, Conceptualization. **Pierson JeanFrançois:** Writing – review & editing, Writing – original draft, Methodology, Investigation. **Alodhayb Abdullah N:** Writing – review & editing, Writing – original draft, Methodology, Funding acquisition, Data curation, Conceptualization.

Declaration of Competing Interest

The authors declare that they have no known competing financial interests or personal relationships that could have influenced the work

reported in this paper.

Acknowledgments

The Authors acknowledge Research Institute Supporting Program (RICSP-26–1), King Saud University, Riyadh, Saudi Arabia.

Data Availability

No data was used for the research described in the article. The data given in the current research are available upon request from the corresponding author.

References

[1] F. Alnjiman, S. Diliberto, J. Ghanbaja, E. Haye, S. Kassavetis, P. Patsalas, C. Gendarme, S. Bruyère, F. Cleymand, P. Miska, Chemical environment and functional properties of highly crystalline ZnSnN2 thin films deposited by reactive sputtering at room temperature, Sol. Energy Mater. Sol. Cells 182 (2018) 30–36, https://doi.org/10.1016/j.solmat.2018.02.037.

[2] N. Yamada, M. Mizutani, K. Matsuura, M. Imura, H. Murata, J. Jia, F. Kawamura, Band gap-tunable (Mg, Zn) SnN_2 earth-abundant alloys with a wurtzite structure, ACS Appl. Electron. Mater. 3 (2021) 4934–4942, https://doi.org/10.1021/acsaelm.1c00754.

[3] T.R. Paudel, W.R.L. Lambrecht, First-principles study of phonons and related ground-state properties and spectra in Zn- IV-N_2 compounds, Phys. Rev. BCondens. Matter Mater. Phys. 78 (2008) 115204, https://doi.org/10.1103/PhysRevB.78.115204.

[4] A. Punya, W.R.L. Lambrecht, M. Van Schilfgaarde, Quasiparticle band structure of Zn-IV-N 2 compounds, Phys. Rev. BCondens. Matter Mater. Phys. 84 (2011) 165204, https://doi.org/10.1103/PhysRevB.84.165204.

[5] A.N. Fioretti, A. Zakutayev, H. Moutinho, C. Melamed, J.D. Perkins, A.G. Norman, M. Al-Jassim, E.S. Toberer, A.C. Tamboli, Combinatorial insights into doping control and transport properties of zinc tin nitride, J. Mater. Chem. C. 3 (2015) 11017–11028, https://doi.org/10.1039/C5TC02663F.

[6] T. Veal, N. Feldberg, N.F. Quackenbush, W.M. Linhart, D.O. Scanlon, L.F.J. Piper, S.M. Durbin, Band gap dependence on cation disorder in ZnSnN2Solar absorber, Adv. Energy Mater. 5 (2015) 1501462, https://doi.org/10.1002/aenm.201501462.

[7] X. Cao, F. Kawamura, Y. Ninomiya, T. Taniguchi, N. Yamada, Conduction-band effective mass and bandgap of $ZnSnN_2$ earth-abundant solar absorber, Sci. Rep. 7 (2017) 14987, https://doi.org/10.1038/s41598-017-14850-7.

[8] P.C. Quayle, K. He, J. Shan, K. Kash, Synthesis, lattice structure, and band gap of ZnSnN2, MRS Commun. 3 (2013) 135–138, https://doi.org/10.1557/mrc.2013.19.

[9] N. Feldberg, B. Keen, J.D. Aldous, D.O. Scanlon, P.A. Stampe, R.J. Kennedy, R.J. Reeves, T.D. Veal, S.M. Durbin, ZnSnN2: A new earth-abundant element semiconductor for solar cells, in: 2012 38th IEEE Photovolt. Spec. Conf., IEEE, 2012: pp. 2524–2527. ⟨https://ieeexplore.ieee.org/abstract/document/6318108⟩.

[10] N. Feldberg, J.D. Aldous, P.A. Stampe, R.J. Kennedy, T.D. Veal, S.M. Durbin, Growth of $ZnSnN_2$ by molecular beam epitaxy, J. Electron. Mater. 43 (2014) 884–888, https://doi.org/10.1007/s11664-013-2962-8.

[11] R.A. Makin, N. Senabulya, J. Mathis, N. Feldberg, P. Miska, R. Clarke, S.M. Durbin, Growth of ordered and disordered $ZnSnN_2$, J. Vac. Sci. Technol. B 35 (2017), https://doi.org/10.1116/1.4978021.

[12] L. Lahourcade, N.C. Coronel, K.T. Delaney, S.K. Shukla, N.A. Spaldin, H.A. Atwater, Structural and Optoelectronic Characterization of RF Sputtered $ZnSnN_2$ (Adv. Mater. 18/2013), Adv. Mater. 25 (2013) 2561, https://doi.org/10.1002/adma.201370120.

[13] D.D. Le, T.S. Ngo, S.-K. Hong, Growth of single crystal non-polar (112 0) ZnSnN2 films on sapphire substrate, Appl. Surf. Sci. 481 (2019) 819–824, https://doi.org/10.1016/j.apsusc.2019.03.195.

[14] F. Deng, H. Cao, L. Liang, J. Li, J. Gao, H. Zhang, R. Qin, C. Liu, Determination of the basic optical parameters of ZnSnN2, Opt. Lett. 40 (2015) 1282–1285, https://doi.org/10.1364/OL.40.001282.

[15] S. Bouhtiyya, R.L. Porto, B. Laïk, P. Boulet, F. Capon, J.P. Pereira-Ramos, T. Brousse, J.F. Pierson, Application of sputtered ruthenium nitride thin films as electrode material for energy-storage devices, Scr. Mater. 68 (2013) 659–662, https://doi.org/10.1016/j.scriptamat.2013.01.030.

[16] A.P. Jaroenjittichai, W.R.L. Lambrecht, Electronic band structure of Mg− IV− N_2 compounds in the quasiparticle-self-consistent GW approximation, Phys. Rev. B 94 (2016) 125201, https://doi.org/10.1103/PhysRevB.94.125201.

[17] B.B. Dumre, D. Gall, S.V. Khare, Stability, and electronic and optical properties of ternary nitride phases of $MgSnN_2$: a first-principles study, J. Phys. Chem. Solids 153 (2021) 110011, https://doi.org/10.1016/j.jpcs.2021.110011.

[18] F. Kawamura, M. Imura, H. Murata, N. Yamada, T. Taniguchi, Synthesis of a novel rocksalt-type ternary nitride semiconductor MgSnN2 using the metathesis reaction under high pressure, Eur. J. Inorg. Chem. 2020 (2020) 446–451, https://doi.org/10.1002/ejic.201901059.

[19] F. Alnjiman, A. Virfeu, D. Pilloud, S. Diliberto, E. Haye, A.E. Giba, S. Migot, J. Ghanbaja, P. Boulet, H. Albrithen, Theoretical and experimental approaches for the determination of functional properties of MgSnN2 thin films, Sol. Energy Mater. Sol. Cells 244 (2022) 111797, https://doi.org/10.1016/j.solmat.2022.111797.

[20] A.L. Greenaway, A.L. Loutris, K.N. Heinselman, C.L. Melamed, R.R. Schnepf, M. B. Tellekamp, R. Woods-Robinson, R. Sherbondy, D. Bardgett, S. Bauers, Combinatorial synthesis of magnesium tin nitride semiconductors, J. Am. Chem. Soc. 142 (2020) 8421–8430, https://doi.org/10.1021/jacs.0c02092.

[21] N. Yamada, K. Matsuura, M. Imura, H. Murata, F. Kawamura, Composition-Dependent Properties of Wurtzite-Type Mg1+ x Sn1–x N2 Epitaxially Grown on GaN (001) Templates, ACS Appl. Electron. Mater. 3 (2021) 1341–1349, https://doi.org/10.1021/acsaelm.0c01115.

[22] A.H. Ramezani, M. Habibi, M. Ghoranneviss, Deposition of magnesium nitride thin films on stainless steel-304 substrates by using a plasma focus device, J. Theor. Appl. Phys. 8 (2014) 175–182, https://doi.org/10.1007/s40094-014-0146-4.

[23] K.Kumar Chinnakutti, V. Panneerselvam, S.T. Salammal, Tailoring optoelectronic properties of earth abundant $ZnSnN_2$ by combinatorial RF magnetron sputtering, J. Alloy. Compd. 772 (2019) 348–358, https://doi.org/10.1016/j.jallcom.2018.08.331.

[24] R. Qin, H. Cao, L. Liang, Y. Xie, F. Zhuge, H. Zhang, J. Gao, K. Javaid, C. Liu, W. Sun, Semiconducting $ZnSnN_2$ thin films for Si/$ZnSnN_2$ pn junctions, Appl. Phys. Lett. 108 (2016), https://doi.org/10.1063/1.4945728.

[25] V. Ramachandran, R.M. Feenstra, W.L. Sarney, L. Salamanca-Riba, J.E. Northrup, L.T. Romano, D.W. Greve, Inversion of wurtzite GaN (0001) by exposure to magnesium, Appl. Phys. Lett. 75 (1999) 808–810, https://doi.org/10.1063/1.124520.

[26] C. Bungaro, K. Rapcewicz, J. Bernholc, Surface sensitivity of impurity incorporation: Mg at GaN (0001) surfaces, Phys. Rev. B 59 (1999) 9771, https://doi.org/10.1103/PhysRevB.59.9771.

[27] P. Wu, T. Tiedje, Molecular beam epitaxy growth and optical properties of Mg3N2 films, Appl. Phys. Lett. 113 (2018), https://doi.org/10.1063/1.5035560.

[28] N. Khemasiri, C. Chananonnawathorn, A. Klamchuen, S. Jessadaluk, A. Pankiew, S. Vuttivong, P. Eiamchai, M. Horprathum, S. Pornthreeraphat, P. Kasamechonchung, Crucial role of reactive pulse-gas on a sputtered Zn 3 N 2 thin film formation, RSC Adv. 6 (2016) 94905–94910, https://doi.org/10.1039/C6RA09972F.

[29] N. Jiang, D.G. Georgiev, A.H. Jayatissa, R.W. Collins, J. Chen, E. McCullen, Zinc nitride films prepared by reactive RF magnetron sputtering of zinc in nitrogen containing atmosphere (https://iopscience.iop.org/article/), J. Phys. D. Appl. Phys. 45 (2012) 135101, https://doi.org/10.1088/0022-3727/45/13/135101/meta.

[30] G.-H. Zhang, X.-Y. Deng, H. Xue, G. Xiang, Engineering of electronic and optical properties of ZnO thin films via Cu doping, Chin. Phys. B 22 (2013) 47803, https://iopscience.iop.org/article/⟨10.1088/1674-1056/22/4/047803/meta⟩.

[31] W.-C. Hsu, Processing-dependent growth mechanisms and performance improvement of kesterite solar cells, University of California, Los Angeles, 2014. ⟨https://www.proquest.com/dissertations-theses/processing-dependent-growth-mechanisms/docview/1513243745/se-2?accountid=44936⟩.

[32] S. Choi, J. Kang, J. Park, Y.-C. Kang, Tin nitride thin films fabricated by reactive radio frequency magnetron sputtering at various nitrogen gas ratios, Thin Solid Films 571 (2014) 84–89, https://doi.org/10.1016/j.tsf.2014.10.035.

[33] F. Ye, R.-T. Hong, Y.-B. Qiu, Y.-Z. Xie, D.-P. Zhang, P. Fan, X.-M. Cai, Nanocrystalline ZnSnN2 prepared by reactive sputtering, its Schottky diodes and heterojunction solar cells, Nanomaterials 13 (2022) 178, https://doi.org/10.3390/nano13010178.